Article

Crystal Chemistry of a New Mineral-like Phosphate Na$_{6.9}$Ni$^{2+}_{0.9}$V$^{3+}_{4.3}$Al$_{0.8}$(PO$_4$)$_8$(H$_2$O)$_2$ in the Series of α-CrPO$_4$ Derivatives

Olga Yakubovich [1,*] , Galina Kiriukhina [1,2] , Valentina Nesterova [3], Anatoly Volkov [4], Stanislav Fedotov [4] and Olga Dimitrova [1]

[1] Department of Crystallography, Lomonosov Moscow State University, Leninskye Gory 1, Moscow 119991, Russia; g-biralo@yandex.ru (G.K.); dimitrova@list.ru (O.D.)

[2] Institute of Experimental Mineralogy RAS, Akademika Osip'yana st 4, Chernogolovka, Moscow 142432, Russia

[3] Department of Mechanical and Materials Engineering, Auburn University, Auburn, AL 36849, USA; vzn0027@auburn.edu

[4] Skoltech Center for Energy Science and Technology, Moscow 121205, Russia; toljha@yandex.ru (A.V.); s.fedotov@skoltech.ru (S.F.)

[*] Correspondence: yakubol@geol.msu.ru; Tel.: +7-9039759106

Abstract: A novel mineral-like phosphate hydrate Na$_{6.9}$Ni$^{2+}_{0.9}$V$^{3+}_{4.3}$Al$_{0.8}$(PO$_4$)$_8$(H$_2$O)$_2$ ($Z = 2$) was obtained under high-temperature hydrothermal conditions by modeling the chemistry of geothermal brines in natural geological solutions. The compound, characterized by scanning electron microscopy and microprobe analysis, possesses an orthorhombic symmetry with the *Cccm* space group; the unit cell parameters are $a = 6.4082(8)$, $b = 19.6813(19)$, $c = 10.5035(11)$ Å. Here we report its crystal structure studied by low-temperature single crystal X-ray diffraction and discussed as derived from the α-CrPO$_4$ archetype, known for a large range of compounds with promising properties. Three-dimensional continuous migration pathways for Na$^+$ within the structure were found and confirmed by a bond valence energy landscape analysis. The migration barriers turned out to be ~0.44 eV along the a and b directions and ~0.42 eV along the c axis. These values suggest that the compound may be a potential electrode material for sodium-ion batteries.

Keywords: mineral-like phosphate hydrate; crystal structure; hydrothermal synthesis; low-temperature X-ray diffraction; α-CrPO$_4$ archetype; structurally related minerals and synthetic phases; sodium migration; cathode material

1. Introduction

Along with oxides, the most common in the Mineral Kingdom, both quantitatively and in terms of species diversity, are natural oxygen-containing phases with complex anions, e.g., silicates, phosphates, vanadates, sulfates, borates, and so on. These minerals hold promising technological potential, thus maintaining the constant interest of the scientific community in designing synthetic analogues and modifying natural oxo salts with cations of transition and alkali metals. Such compounds are widely used as catalysts, sorbents, molecular sieves, and ion exchangers, as well as in various magnetic materials and resources for energy technologies, in particular, as the basis of electrodes in portable energy sources, etc. [1–4]. Particularly, large availability and distribution of phosphates in the Earth's crust, where they occupy third place after silicates and oxides, guarantee low cost and environmental safety of their laboratory synthesized counterparts [5,6].

Data on mineral crystal genesis contains important information about the conditions under which a particular structure can form. Chemical compositions of minerals—natural inorganic compounds—indicate the types of cations (and anions) that can form a stable crystal structure, and the results of X-ray diffraction analysis provide information about preferred crystallographic positions for certain atoms. Experimental laboratory studies make it possible to establish the limits of miscibility of solid solutions and outline the ways to control cationic ordering, defect concentrations, and oxidation state of ions, which is important for creating electrochemically active, catalytic, magnetic, and other functional materials.

Many modern renewable energy sources use large batteries to adjust frequency and vary peak performance. For such stationary devices, service life, power, price, and availability of materials are critical. Sodium ion batteries meet these criteria. Na ranks seventh in the elemental content of the Earth's crust; its global amount (23,000 ppm) is extremely high. The close properties of Li and Na as alkali metals are used to develop sodium-ion batteries based on the operating principles and manufacturing techniques of well-designed lithium-ion devices. Sodium ion (Na^+) is heavier and has a larger ionic radius than lithium ion (Li^+), and therefore Na-ion batteries are not expected to compete with the Li-ion technology in terms of volumetric and gravimetric energy density, but it is likely that the Na rich resources will be used to ensure cost attractiveness and complement Li-ion batteries in large scale applications [7–11]. Notably, Na ions can exhibit a higher diffusion in crystal structures compared to Li ions. This leads to a higher power density of these types of batteries, which look like a reasonable solution to replace toxic lead-acid counterparts.

The extensively studied candidates for battery application are phosphate-based materials, among which vanadium phosphates are known as high efficiency positive electrodes (cathodes). Vanadium can form a number of electrochemically active redox couples (V^{4+}/V^{5+}, V^{3+}/V^{4+}, and V^{2+}/V^{3+}) offering wide tunability as to chemical compositions and redox potentials [12]. Particularly, fluoride-phosphates with the general formula $Na_3V_2(PO_4)_2F_{3-2y}O_{2y}$ turned out to be the most attractive: they demonstrate outstanding performance in Na-ion cells, providing an energy density of ~500 W h kg^{-1} which is comparable with the performance of commercial Li-ion battery cathodes [13]. In the search for such compounds, we obtained a mineral-like phosphate, which is discussed here as a derivative of the α-$CrPO_4$ structure type [14].

2. Materials and Methods

2.1. Hydrothermal Synthesis

Micron-size single crystals of the compounds (Figure 1) were obtained under high-temperature hydrothermal conditions. To simulate the chemistry of geothermal brines in natural geological solutions, we used chemically pure reagents $AlCl_3$:$NiCl_2$:VCl_3:NaH_2PO_4 components in a weight ratio of 1:1:2:3, which corresponded to 7.5 mmol of $AlCl_3$, 7.7 mmol of $NiCl_2$, 12.7 mmol of VCl_3, and 25 mmol of NaH_2PO_4.

Subsequently, all components were dissolved in 10 mL of distilled water; the resulting solution was transferred to a 20 mL copper-lined nickel–chromium alloy autoclave. To preserve the oxidation state, a small amount of citric acid (0.25 g) was added to the vanadium-containing samples. The autoclaves were closed and placed in a furnace, where they were heated to 673 K for 24 h and kept at this temperature and a pressure of 50 MPa for 10 days. The pressure in the system was calculated based on the filling factor of the autoclave; it gradually increased with increasing temperature. It is critical for safety reasons to use superalloy autoclaves, as the creep rupture stress significantly enlarges with the increase in temperature. After the reaction, the autoclave was allowed to cool naturally for several hours. The precipitate was separated by filtration, washed with hot distilled

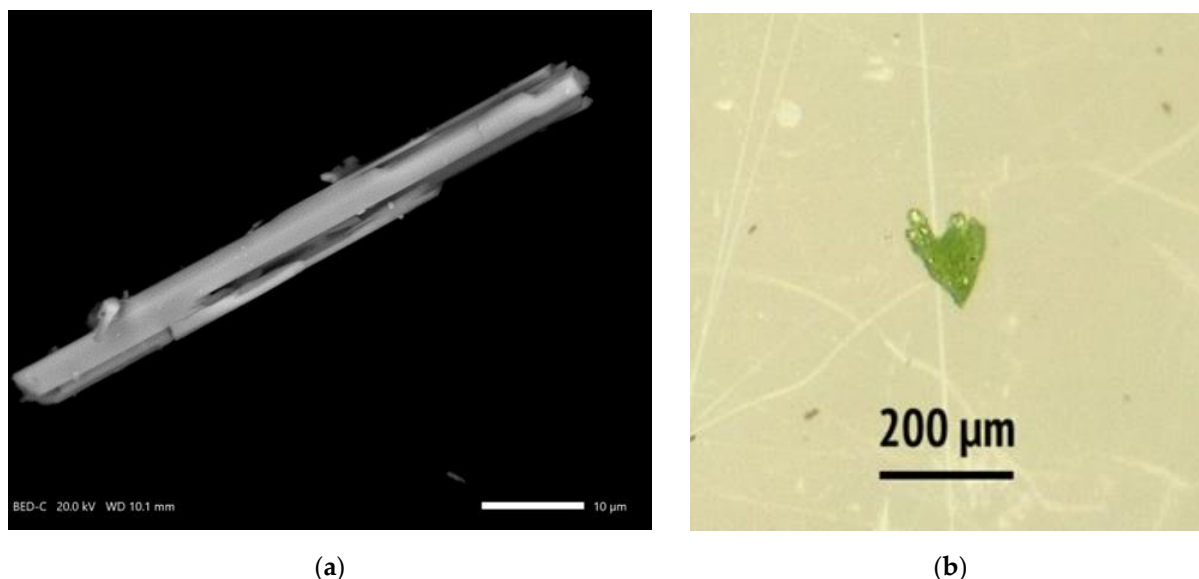water, dried at room temperature for 12 h, and examined for the chemical composition and crystal structure.

(**a**)   (**b**)

Figure 1. (**a**) Secondary-electron SEM image, showing sample morphology; (**b**) Photograph of a crystals' drusen.

2.2. X-Ray Energy-Dispersive Analysis

Obtained crystals of the presumably new phase were analyzed with a scanning electron microscope (SEM), i.e., a JEOL JSM-6480LV Oxford X-Max^N equipped with an energy-dispersive X-ray (EDX) spectrometer. The unpolished surface of the crystal was covered with a carbon film of about 25 nm thickness. To minimize the thermoelectric effect of the electron probe, leading to dehydration and intense migration of low-charged sodium cations outside the interaction region, the probe current and electrical load per unit area of the samples were reduced using the fast scan mode for relatively large surface areas. The measurement conditions were optimized with an acceleration voltage of 20 kV and a current of 10 nA, at which the sample was stable; the spectrum acquisition time was 50 s.

2.3. Single-Crystal X-Ray Diffraction

The X-ray diffraction data were acquired at 110 K for the single crystal on a Bruker APEX-II CCD diffractometer using Mo-K_α radiation. The intensities of reflections were corrected for background, Lorentz and polarization effects, and absorption [15]. Most calculations for the structural study were performed with the WinGX program system [16]. The crystal structure was solved via direct methods and refined against the F^2 data using the SHELX programs [17,18]. Atomic scattering factors and anomalous dispersion corrections were taken from the "International Tables for Crystallography" [19]. Structural data were deposited via the joint CCDC/FIZ Karlsruhe deposition service under the deposition number 2,405,079. Cif-data can be obtained free of charge from FIZ Karlsruhe. The cif and checkcif files can also be found in the Supplementary Materials to this paper.

3. Results and Discussion

3.1. Chemical Composition

The energy-dispersive X-ray (EDX) microanalysis of light-green prismatic crystals showed the presence of Na, Ni, V, Al, P, and O atoms according to their principal *K*-shell emission lines.

3.2. Crystal Structure Solution

Crystal data and details of data collection and refinement are presented in Table 1. The orthorhombic phase with unit-cell parameters a = 6.4082(8), b = 19.681(2), c = 10.504(1) Å crystallizes in the space group *Cccm*. In the course of the structure solution, two symmetrically independent positions in octahedral surroundings of O atoms were found. According to the coordination geometry and the chemical compositions, these structural sites were supposed to be mixed, populated by V/Ni and V/Al atoms. Our refinement has shown that the 8h position at the two-fold rotation axis is statistically occupied by V^{3+} and Ni^{2+} (*M*1), while the 4f Wykoff position at the inversion center adopts V^{3+} and Al (*M*2). We also found two pairs of split Na sites and one Na site that is partly populated.

Table 1. Crystal data and details of the X-ray data collection and refinement for $Na_{6.9}Ni^{2+}_{0.9}V^{3+}_{4.3}Al_{0.8}(PO_4)_8(H_2O)_2$.

Crystal Data	
Formula weight	2500.51
Crystal system, space group	Orthorhombic, *Cccm*
Unit cell parameters, Å	a = 6.4082(8)
	b = 19.6813(19)
	c = 10.5035(11)
Volume, Å^3	1324.7(3)
Z, Calculated density, g/cm^3	2, 3.134
Crystal size, mm	$0.042 \times 0.155 \times 0.437$
Data Collection	
Radiation	Mo-K_α, graphite monochromator
Temperature, K	110(2)
Scanning mode	ω
Measuring range	max θ = 29.99°
Reflections (total)	6683
R_{int}, R_σ	0.1084, 0.0620
Refinement	
Refinement method	Full-matrix least-squares on F^2
Reflections unique/observed	1025/804
Parameters	89
Absorption correction, T_{max}/T_{min}	Numerical, 0.648/0.536
Goodness-of-fit, S	1.109
Residuals [I > 2sigma(I)]	$R1$ = 0.0516, w$R2$ = 0.1073
$\Delta\rho$ (max/min), e/Å^3	0.862 and −0.794

One of the localized O atoms was supposed to form a water molecule, due to its non-bonded character. This oxygen atom was refined as statistically distributed between two structural sites at a short O−O distance of 0.92(4) Å. The corresponding hydrogen atom was located via the electron density difference synthesis, and its coordinates were refined. The crystal structure was refined to R = 0.0516 using anisotropic displacement parameters for all non-hydrogen atoms. The refinement resulted in the crystal chemical formula $Na_{3.46}(V^{3+}_{1.54}Ni^{2+}_{0.46})^{M1}(V^{3+}_{0.61}Al_{0.39})^{M2}(PO_4)_4(H_2O)$ (Z = 4), which reflects a distribution of cations between two positions (*M*1 and *M*2) in the octahedra. The simplified formula for Z = 2 can be written as $Na_{6.9}Ni^{2+}_{0.9}V^{3+}_{4.3}Al_{0.8}(PO_4)_8(H_2O)_2$. In Table 1, we report the crystallographic characteristic of the title compound and the experimental conditions of data collection and refinement. Table 2 presents the final atomic positions and equivalent displacement parameters. Characteristic distances are given in Table 3. The data of bond valence calculations [20], exposed in Table 4, are consistent with the assumed oxidation state of V and Ni. Most figures displaying crystal structures were made with the Diamond program [21].

Table 2. Atomic coordinates and equivalent anisotropic displacement parameters for $Na_{6.9}Ni^{2+}_{0.9}V^{3+}_{4.3}Al_{0.8}(PO_4)_8(H_2O)_2$.

Atom	x	y	z	U_{iso} */U_{eq}	Occ. (<1)
V1	0.750000	0.750000	0.500000	0.0102(5)	0.609(15)
Al1	0.750000	0.750000	0.500000	0.0102(5)	0.391(15)
V2	0.000000	0.65880(5)	0.750000	0.0105(3)	0.787(17)
Ni1	0.000000	0.65880(5)	0.750000	0.0105(3)	0.213(17)
P1	0.8422(3)	0.58964(8)	0.500000	0.0122(4)	
P2	0.500000	0.70237(8)	0.250000	0.0128(4)	
O1	0.5403(5)	0.75461(15)	0.3611(3)	0.0133(7)	
O2	0.3126(5)	0.65892(15)	0.2849(3)	0.0166(7)	
O3	0.7066(7)	0.6539(2)	0.500000	0.0188(10)	
O4	0.9847(6)	0.58914(17)	0.6170(3)	0.0231(8)	
O5	0.7004(8)	0.5290(3)	0.500000	0.0391(16)	
O6	0.572(3)	0.500000	0.750000	0.104(10)	0.5
Na1	0.8413(18)	0.500000	0.750000	0.032(2)	0.351(5)
Na2	0.245(2)	0.7844(9)	0.500000	0.057(7)	0.252(12)
Na3	0.1606(7)	0.9072(3)	0.500000	0.0362(13)	0.660(4)
Na4	0.133(2)	0.9366(8)	0.5880(15)	0.0362(13)	0.170(4)
Na5	0.000000	0.500000	0.750000	0.032(2)	0.298(10)
H1	0.679(6)	0.519(4)	0.783(7)	0.150 *	0.5

* H1 atom has been refined in an isotropic approximation.

Table 3. $Na_{6.9}Ni^{2+}_{0.9}V^{3+}_{4.3}Al_{0.8}(PO_4)_8(H_2O)_2$. Characteristic distances, Å.

P1—tetrahedron		P2—tetrahedron		M1 *—octahedron		M2 **—octahedron		Na1—seven-vertex polyhedron	
P1—O5	1.499(5)	P2—O2	1.519(3) × 2	M1—O4	1.960(3) × 2	M2—O3	1.911(5) × 2	Na1—O4	2.423(6) × 2
—O4	1.532(3) × 2	—O1	1.577(3) × 2	—O2	2.037(3) × 2	—O1	1.985(3) × 4	—O4′	2.503(6) × 2
—O3	1.535(5)			—O1	2.082(3) × 2			—O6	2.65(2)
								—O5	2.835(4) × 2

Na2—octahedron		Na3—seven-vertex polyhedron		Na4—octahedron		Na5—octahedron	
Na2—O1	2.46(1) × 4	Na3—O5	2.410(8)	Na4—O5	2.09(2)	Na5—O4	2.245(3) × 4
—O2	2.548(9) × 2	—O4	2.584(6) × 2	—O2	2.33(2)	—O6	2.75(2) × 2
		—O2	2.614(4) × 2	—O5	2.42(1)		
		—O5	2.632(8)	—O6	2.48(2)		
		—O3	2.644(7)	—O4	2.52(1)		
				—O3	2.96(1)		

* $M1(V^{3+}_{1.54}Ni^{2+}_{0.46})$. ** $M2(V^{3+}_{0.61}Al_{0.39})$.

Table 4. Bond valence data for $Na_{6.9}Ni^{2+}_{0.9}V^{3+}_{4.3}Al_{0.8}(PO_4)_8(H_2O)_2$ *.

Atom	M1	M2	P1	P2	Na1	Na2	Na3	Na4	Na5	H1	Σ
O1	$0.385_{↓2}$	$0.474_{↓4}$		$1.114_{↓2}$		$0.021_{↓4→2}$					1.99
O2	$0.435_{↓2}$			$1.303_{↓2}$		$0.017_{↓2}$	$0.074_{↓2}$	0.082			1.91
O3		$0.580_{↓2}$	1.248				0.068	0.015			1.91
O4	$0.536_{↓2}$		$1.258_{↓2}$		$0.107_{↓2}$ $0.132_{↓2}$		$0.080_{↓2}$	0.050	$0.051_{↓4}$		2.22
O5			1.376		$0.043_{↓2→2}$		0.070 0.128	$0.166_{→2}$ $0.064_{→2}$		0.085	2.20
O6 (H₂O)					0.072			0.054	$0.022_{↓2}$	0.415	0.56
Σ	2.71	3.06	5.14	4.83	0.64	0.12	0.64	0.41	0.25	0.5	

* $M1(V^{3+}_{1.54}Ni^{2+}_{0.46})$, $M2(V^{3+}_{0.61}Al_{0.39})$. The bond valence sums calculated for the sodium atoms and water molecules reflect the statistical occupancy of structural positions by them (see text). Symbols → and ↓ denote an increase in the corresponding contributions in rows and columns due to symmetry.

3.3. Crystal Chemistry in Comparison with Related Minerals and Synthetic Analogues

3.3.1. Analysis of Interatomic Distances and Crystal Structure Description

Figure 2 shows the basic structural units of the anionic framework. Both symmetrically independent octahedra are mainly occupied by V^{3+} ions, which are "diluted" by Ni^{2+} [$M(1)$], or Al^{3+} cations [$M(2)$]. In the $M(1)O_6$ octahedra with C_2 symmetry and the V:Ni = 3:1, three

pairs of $M(1)$—O distances are equal to 1.960(3), 2.037(3), and 2.082(3) Å (average 2.026 Å). The centrosymmetric $M(2)O_6$ octahedra populated by V and Al atoms in a ratio of 3:2 are obviously smaller, with four equal $M(2)$—O distances of 1.986(3) Å and two shorter ones of 1.912(5) Å (average 1.961 Å). The $P(1)O_4$ tetrahedra with C_m symmetry are characterized by two P—O bond lengths of 1.532(3) and two others of 1.499(5) and 1.534(5) Å. Strongly distorted $P(2)O_4$ tetrahedra at the two-fold axis have two P—O bond lengths equal to 1.519(3) Å and two larger ones of 1.577(3) Å. The shortest $P(1)$—O distances of 1.499(5) Å correspond to "pendant" oxygen vertices in the tetrahedra, not shared with polyhedra forming a mixed anionic framework (Table 3).
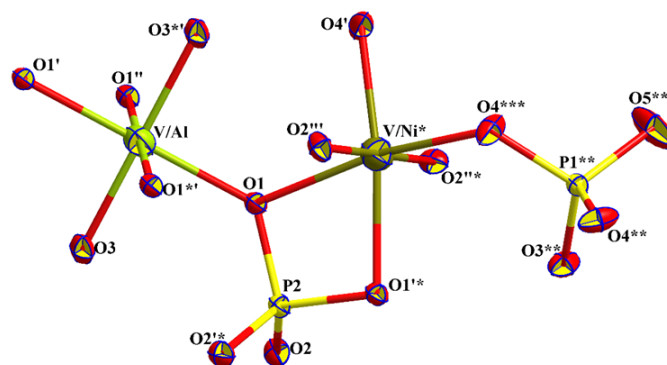

Figure 2. Basic structural units with an atom labelling scheme. Displacement ellipsoids are represented at the 90% probability level. Symmetry code: (′) $1.5 - x, 1.5 - y, 1 - z$; (″) $x, y, 1 - z$; (‴) $0.5 + x, 1.5 - y, 0.5 - z$; (*) $0.5 - x, 0.5 - y, 1 - z$; (**) $-0.5 + x, 1.5 - y, 0.5 - z$; (***) $-0.5 + x, 1.5 - y, -0.5 + z$; (′*) $1 - x, y, 0.5 - z$; (*′) $1.5 - x, 1.5 - y, z$; (″*) $0.5 - x, 1.5 - y, z$.

Intercrossed chains built by alternating $M(1)$- and $M(2)$-centered octahedra linked via oxygen-bridging contacts are aligned in the [101] and [$\bar{1}$01] directions (Figure 3a). Each $M(2)O_6$ polyhedron, jointly occupied by V and Al atoms, shares four O vertices with neighboring $M1O_6$ octahedra that are jointly populated by V and Ni atoms. Alternatively, every $M(1)O_6$ polyhedron shares two O vertices with $M(2)O_6$ octahedra (Figure 3b) to form two-layered slabs perpendicular to the b axis of the unit cell at $y = \frac{1}{4}$ and $\frac{3}{4}$. $P(2)O_4$ tetrahedra share all vertices and one edge with octahedra within the slabs, while one vertex of $P(1)O_4$ tetrahedra is not shared with octahedra and is directed along the b axis in the space between the slabs (Figure 3c).
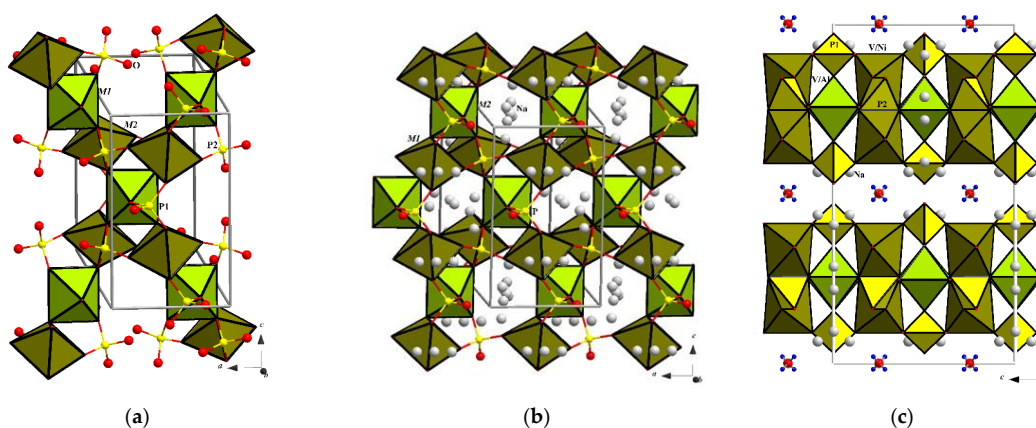

| (a) | (b) | (c) |

Figure 3. (**a**) Intercrossed chains of octahedra strengthened by orthophosphate tetrahedra in the $Na_{6.9}Ni^{2+}_{0.9}V^{3+}_{4.3}Al_{0.8}(PO_4)_8(H_2O)_2$ crystal structure; (**b**) Two-layered slab formed by MO_6 octahedra and PO_4 tetrahedra displaced along the [010] direction with Na atoms in the interstices; (**c**) The title structure in the yz projection.

A bi-periodic anionic network with the formula $[Ni^{2+}_{0.9}V^{3+}_{4.3}Al_{0.8}(PO_4)_8]^{6.9-}$ is neutralized by Na^+ cations mostly distributed in the free space between the slabs (Figure 4a). All Na atoms are disordered in the structure. Thus, Na5 lies in a special position, *4b*, with D_2 symmetry and is surrounded by four O4 and two H_2O ligands forming octahedra. The Na1 atoms in seven-vertex polyhedra on a 2-fold axis (a special position *8g*) are at a forbidden distance Na1 − Na5 = 1.02(1) Å. Our refinement has shown that Na1 and Na5 statistically occupy their sites in a ratio of 0.70:0.30. Similarly, Na3 and Na4 atoms with C_m and C_1 symmetry, respectively, are displaced at 1.10(1) Å from each other; they occupy the structural sites in a ratio of 0.66:0.34. The Na3 atoms accommodate seven-vertex polyhedra, while Na4 atoms are in an octahedral surrounding of five O and one H_2O ligand. The $Na2O_6$ polyhedra with C_m symmetry are statistically populated for 25% (Figure 4a). The H_2O molecules between the slabs of MO_6 octahedra and PO_4 tetrahedra link the slabs via hydrogen bonds (Table 5). Together with the sodium atoms, the H bonds connect neighboring two-periodic anionic structural fragments along the *b* axis (Figure 4b).
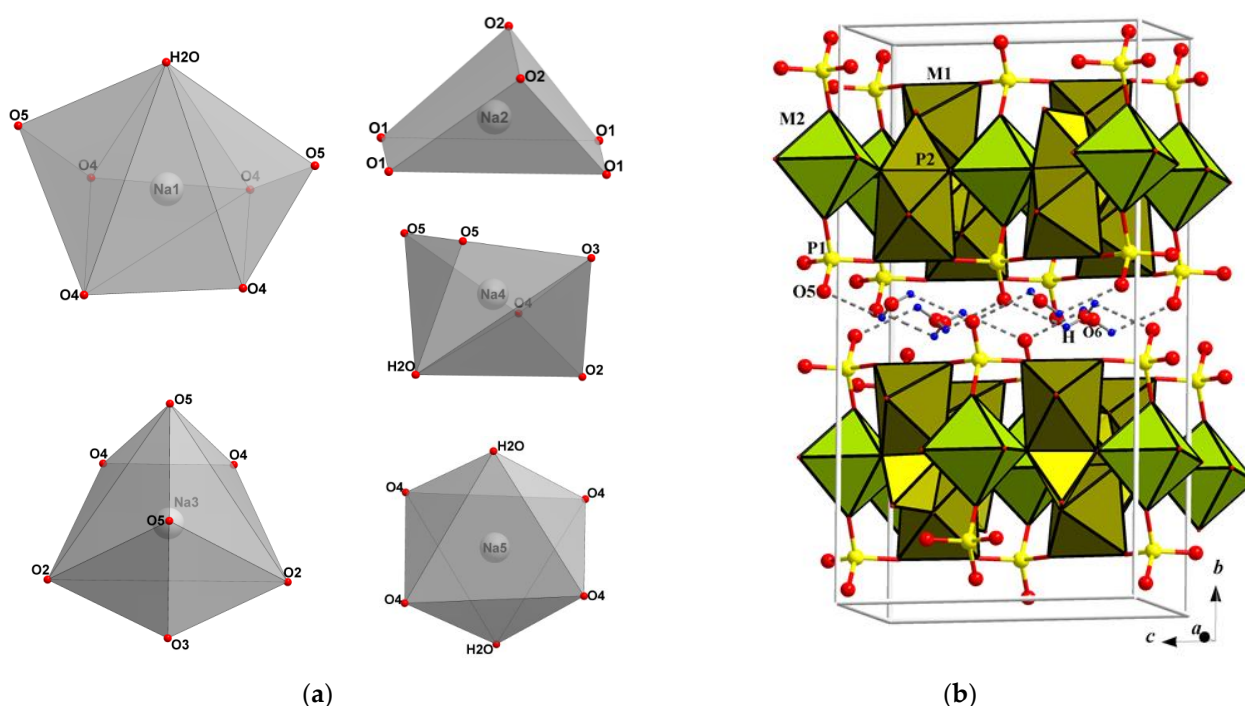

(**a**)   (**b**)

Figure 4.   (**a**) Na-centered polyhedra formed by O and H_2O ligands; (**b**) The $Na_{6.9}Ni^{2+}_{0.9}V^{3+}_{4.3}Al_{0.8}(PO_4)_8(H_2O)_2$ crystal structure shown along the *a* axis. The hydrogen bonds O6 –H1······O5 acting between bi-periodic slabs of the $Ni^{2+}_{0.9}V^{3+}_{4.3}Al_{0.8}(PO_4)_8$ composition are exposed.

Table 5. H-bonding in $Na_{6.9}Ni^{2+}_{0.9}V^{3+}_{4.3}Al_{0.8}(PO_4)_8(H_2O)_2$.

D—H······*A*	*D*—H, Å	H······*A*, Å	*D*······*A*, Å	angle *D*—H···*A*, °
O6—H1······O5	0.850(1)	2.47(9)	2.811(6)	105(7)

3.3.2. Structurally Related Synthetic and Mineral Phases

The α-$CrPO_4$ crystal structure is known as the archetype for a large range of compounds with promising properties. In particular, the hollow structure of α-VPO_4 [22] and $NaV_3(PO_4)_3$ demonstrates a high reversible capacity and excellent cycling stability, attributed to its ability to accommodate alkaline metal ions within its structural channels. At the same time, the $NaVPO_4F$ [23] and $NaVOPO_4$ [24] compounds adopt a KTP structure closely related to α-$CrPO_4$. These materials display several advantages, including high average operating potential, excellent structural stability, and superior rate capability. It

makes them promising candidates for use as cathode materials in sodium-ion batteries. Additionally, incorporating specific cations or transition metals can significantly enhance their conductive properties.

The first "stuffed" α-$CrPO_4$-type structure $NaV^{2.67+}_3(PO_4)_3$ was described by Kinomura et al. in 1989 [25]. The $NaV_3(PO_4)_3$ represents an anode material for Na-ion batteries, which exhibits a high reversible capacity of 140 mA h g^{-1} with the capacity retention of about 98% after 100 cycles [26]. In addition, this material demonstrates required thermal stability up to $\sim$450 °C in the charged state, which is critical for long-term cycling and large-scale applications. The transport mechanism of Na$^+$ is cooperative diffusion along the *b*- or *c*-axis [27]. At the moment, numerous isotypic phosphates with first-row transition metals and some arsenates were synthesized and studied.

Cr atoms occupy two symmetrically independent positions in the oxygen environment in the α-$CrPO_4$ crystal structure. When introducing two different transition metals in the crystallization system, these atoms usually orderly populate the 4*a* and 8*g* structural sites within the *Imma* space group to form compounds with a common formula Na$AB_2(TO_4)_3$, where *A* and *B* denote fist-raw transition metals, and *T* indicates P or As. These crystal structures represent $[AB_2(TO_4)_3]^-$ anionic frameworks neutralized by Na$^+$ ions. When the amount of Na atoms becomes higher, or K atoms also participate in the phase composition, the crystal structure changes for bi-periodic double layers with K, Na atoms, and H_2O molecules between the slabs (Table 6). The structure transformation is accompanied by an increase of one parameter of the unit cell, its volume, and space group change.

In Table 6 we have summarized minerals with crystal structures derived from the α-$CrPO_4$ archetype and the laboratory obtained structurally related V-containing phosphates prioritized for our study. Most synthetic phases are orthorhombic and crystallize in the similar body-centered space group *Imma* as their isostructural prototypes α-$CrPO_4$ and VPO_4. These compounds with body-centered unit cells are characterized by so-called "stuffed α-$CrPO_4$" structures with a tri-periodic framework made of octahedra and tetrahedra that are sharing corners and/or edges, generating channels parallel to the [100] and [010] directions, in which the sodium atoms are located, whereas in the α-$CrPO_4$ the corresponding channels are vacant. A similar crystal structure is inherent to the yakubovichite, $CaNi_2Fe^{3+}(PO_4)_3$ [28], a rare representative of a natural Ni phosphate and a unique mineral that obeys the "stuffed" α-$CrPO_4$ type (A synthetic analogue of yakubovichite, $CaNi_2Fe^{3+}(PO_4)_3$, is known (see Ouatta et al. 2017 [29])). According to [28], the association with Ni-phosphides—negevite NiP_2, halamishite Ni_5P_4 and transjordanite Ni_2P—indicates the yakubovichite formation during pyrolytic oxidation (dry roasting) of these minerals. The following process could be accompanied by side reactions with Ca-bearing phases—calcite, lime, or fluorapatite,—which served as a source of Ca [28].

One more mineral, sverigeite, $Na(Mn_{1.37}Mg_{0.63})SnBe_2(SiO_4)_3(OH)$ [30], is characterized by the same orthorhombic body-centered space group *Imma* that is inherent to the α-$CrPO_4$, and close unit cell parameters to the parameters of the α-$CrPO_4$ "stuffed" derivatives (Table 6). The sverigeite crystal structure includes SnO_6 and $(Mn, Mg)O_6$ octahedra, strongly corrugated beryllosilicate chains built from 3- and 4-membered rings, and Na atoms. A rewritten formula of sverigeite, $[NaBe_2(OH)]Mn_2Sn(SiO_4)_3$ reveals its structural similarity with yakubovichite, $[Ca]Ni_2Fe(PO_4)_3$ as shown in Figure 5. In spite of significantly different compositions of these minerals, their crystal structures can be considered as designed using the same bi-periodic modules, which have been highlighted in the α-$CrPO_4$ archetype structure (Figure 6).
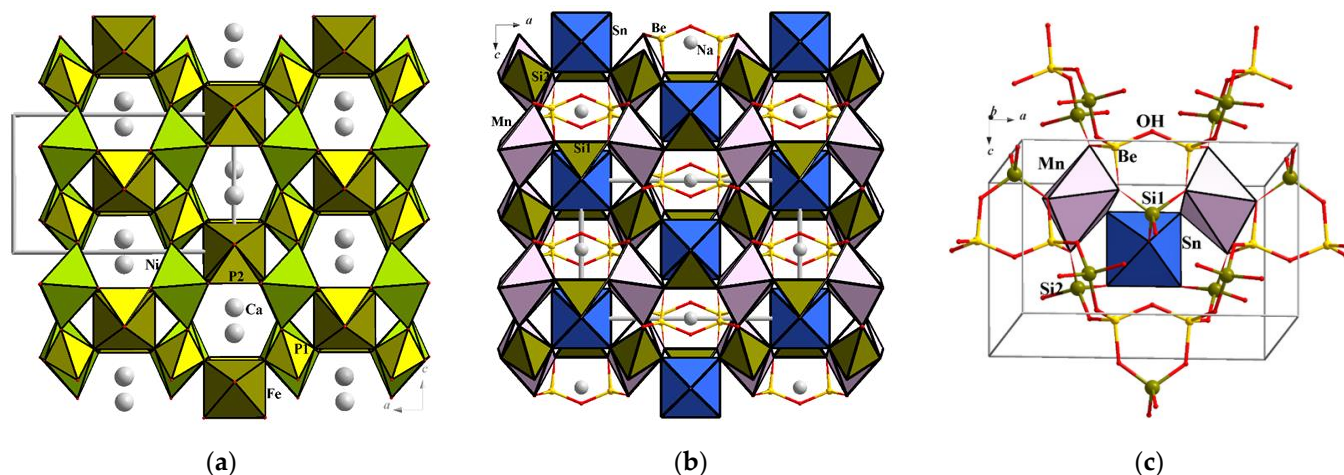
Figure 5. The crystal structures of (**a**) phosphate mineral yakubovichite, (**b**) beryllosilicate sverigeite in *xz* projections, and (**c**) the fragment of sverigeite crystal structure showing corrugated chains formed by SiO_4 and BeO_3OH tetrahedra.
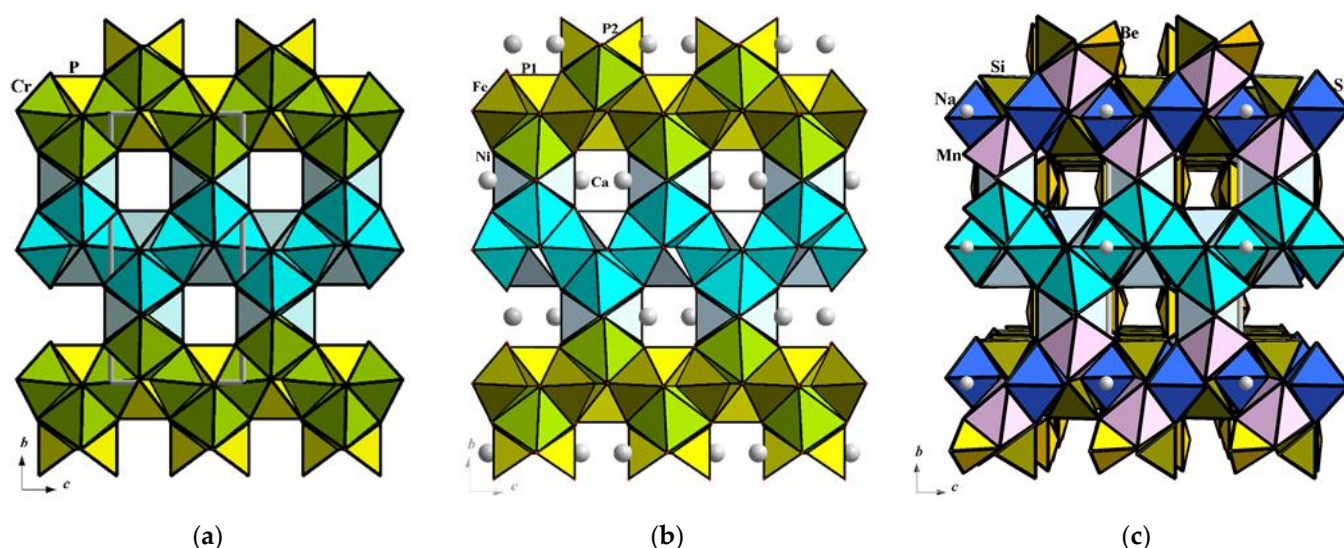

Figure 6. The crystal structures of (**a**) α-$CrPO_4$, (**b**) yakubovichite and (**c**) sverigeite exposed in *yz* projections. The repeating structural fragments, i.e., modules built from octahedra (cyan) and tetrahedra (light blue), are highlighted.

As we mentioned before, the amount of extra framework atoms and their size regulate structural changes from tri-periodic frameworks to bi-periodic slabs (double layers) and by increasing the unit cell axis perpendicular to the slabs. This process associates with a reduction in body-centered cells to face-centered, or primitive, and even with a decrease in symmetry to monoclinic. The $Na_{6.9}Ni^{2+}_{0.9}V^{3+}_{4.3}Al_{0.8}(PO_4)_8(H_2O)_2$ crystal structure can be considered as an illustration for this kind of transformation from the framework to layered construction, where double-layered modules built by octahedra and tetrahedra alternate with Na atoms and water molecules. Another example of the framework structure conversion can be noticed in connection with a hydrated layered vanadium (III) phosphate, $K_3V_3(PO_4)_4 \cdot H_2O$ [31]. A primitive *Pnna* orthorhombic unit cell with the *b* parameter equal to 20.850(1) Å, is assigned to the compound with layers of corner-sharing VO_6 octahedra linked by corners and edges with PO_4 tetrahedra forming a hydrated K^+ ion interlayer. The crystal structure and thermal stability of this hydrated phase suggest that it may be a suitable alkali cation intercalation host for K^+ ions and alternative alkali ions. This suggestion is supported by the exhibited electrochemical activity of $K_3V_3(PO_4)_4 \cdot H_2O$

vs. K/K$^+$, displaying characteristic charge and discharge plateaus at 3.7–3.9 and 3.6 V, respectively. A monoclinic reduction (space group *C2/c*) from the orthorhombic *Imma* symmetry has been found in the Na$_3$V^{3+}$_3$(PO$_4$)$_4$ layered structure with a tri-periodic Na$^+$ ion channel allowing excellent cycling and rate performance (92% of its capacity is retained after 100 electrochemical cycles). According to [32], the voltage profiles of Na$_3$V$_3$(PO$_4$)$_4$ show that it can reversibly uptake nearly one Na$^+$ ion with a 3.9 V voltage plateau, which is the highest value among Na-containing V-based orthophosphates ever reported.

Table 6. Crystal chemical data for synthetic V-bearing phosphates and structurally related minerals, based on the α-CrPO$_4$ archetype.

Compound/Mineral	Unit Cell Parameters, Å	Space Group; *Z*; *V*, Å^3	Crystal Structure Description	Ref.
		α-CrPO$_4$ archetype		
α-CrPO$_4$	a = 10.403(2) b = 12.898(2) c = 6.299(1)	*Imma* 12 845.19	CrPO$_4$ tri-periodic framework	[14]
		Synthetic V-bearing phosphates		
α-VPO$_4$	a = 10.5591(1) b = 13.1051(1) c = 6.33928(7)	*Imma* 12 877.22(2)	VPO$_4$ tri-periodic framework	[22]
NaV$^{2.67+}$$_3$(PO$_4$)$_3$	a = 10.488(2) b = 13.213(3) c = 6.455(1)	*Imma* 4 894.52	[V$^{2.67+}$$_3$(PO$_4$)$_3$]$^-$ anionic tri-periodic framework with Na$^+$ ions in the channels	[25]
NaFeV$_2$(PO$_4$)$_3$	a = 10.5067(4) b = 13.2437(6) c = 6.3946(2)	*Imma* 4 889.80(6)	[Fe^{2+}V^{3+}$_2$(PO$_4$)$_3$]$^-$ anionic tri-periodic framework with Na$^+$ ions in the channels	[33]
NaCoV$_2$(PO$_4$)$_3$	a = 10.495(1) b = 13.184(1) c = 6.3920(6)	*Imma* 4 884.4(1)	[Co^{2+}V^{3+}$_2$(PO$_4$)$_3$]$^-$ anionic tri-periodic with Na$^+$ ions in the channels	[33]
NaNiV$_2$(PO$_4$)$_3$	a = 10.5091(5) b = 13.1212(5) c = 6.3540(3)	*Imma* 4 876.16(6)	[Ni^{2+}V^{3+}$_2$(PO$_4$)$_3$]$^-$ anionic tri-periodic with Na$^+$ ions in the channels	[33]
Na$_{3.46}$(V^{3+}$_{1.54}$Ni^{2+}$_{0.46}$)^{M1} (V^{3+}$_{0.61}$Al$_{0.39}$)^{M2}(PO$_4$)$_4$(H$_2$O)	a = 10.504(1) b = 19.681(2) c = 6.4082(8)	*Amaa* * 4 1324.7(3)	[Ni^{2+}$_{0.46}$V^{3+}$_{2.15}$Al$_{0.39}$(PO$_4$)$_4$]$^{3.46-}$ bi-periodic anionic slabs (double layers) joint together by Na$^+$ ions and hydrogen bonds	This work
K$_3$V^{3+}$_3$(PO$_4$)$_4$·H$_2$O	a = 10.7161(4) b = 20.850(1) c = 6.5316(2)	*Pnna* 4 1459.36	[V^{3+}$_3$(PO$_4$)$_4$]$^{3-}$ bi-periodic anionic slabs (double layers) joint together by K$^+$ ions and hydrogen bonds	[31]
Na$_3$V^{3+}$_3$(PO$_4$)$_4$	a = 19.6724(4) b = 6.4041(1) c = 10.5890(2) β = 91.967(2)	*C2/c* 4 1323.24	[V^{3+}$_3$(PO$_4$)$_4$]$^{3-}$ bi-periodic anionic slabs (double layers) joint together by Na$^+$ ions	[32]
		Minerals		
Yakubovichite CaNi$_2$Fe^{3+}(PO$_4$)$_3$	a = 10.388(1) b = 13.088(1) c = 6.4794(6)	*Imma* 4 880.94(2)	[Ni$_2$Fe^{3+}(PO$_4$)$_3$]$^{2-}$ anionic tri-periodic framework with Ca^{2+} ions in the channels	[28]
Ozerovaite, Na$_2$K(Al$_{1.64}$Fe^{3+}$_{0.36}$)(AsO$_4$)$_4$	a = 10.615(2) b = 20.937(3) c = 6.3932(9)	*Cmca* 4 1420.9(3)	[(Al, Fe^{3+})(AsO$_4$)$_4$]$^{3-}$ bi-periodic anionic slabs (double layers) joint together by Na$^+$ and K$^+$ ions	[34]
Pansnerite, Na$_{1.6}$K$_{1.4}$(Fe^{3+}$_{1.65}$Al$_{1.35}$)(AsO$_4$)$_4$	a = 10.7372(3) b = 20.8367(8) c = 6.4734(2)	*Cmca* 4 1448.27(7)	[(Fe^{3+}, Al) (AsO$_4$)$_4$]$^{3-}$ bi-periodic anionic slabs (double layers) joint together by Na$^+$ and K$^+$ ions	[35]
Sverigeite, Na(Mn$_{1.37}$Mg$_{0.63}$)SnBe$_2$ (SiO$_4$)$_3$(OH)	a = 10.815(8) b = 13.273(8) c = 6.818(6)	*Imma* 4 978.71(7)	[(Mn, Mg)SnBe$_2$(SiO$_4$)$_3$OH]$^-$ tri-periodic framework with Na$^+$ ions in the channels	[30]

* A non-standard setting of the space group *Cccm* is given for uniformity of the unit cell parameters.

The structural derivatives from the α-CrPO$_4$ archetype, discussed above, characterized by unit cell volumes lying in the approximate range of 1320–1460 Å^3, have similar crystal structures formed by bi-periodic modules built from octahedra and tetrahedra interlayered with alkali ions and water molecules. These topologically identical modules represent fragments "extracted" from the parent α-CrPO$_4$ structure, where they are directly connected via common edges and vertices of polyhedra adjacent along the largest unit cell axis (Figure 7).
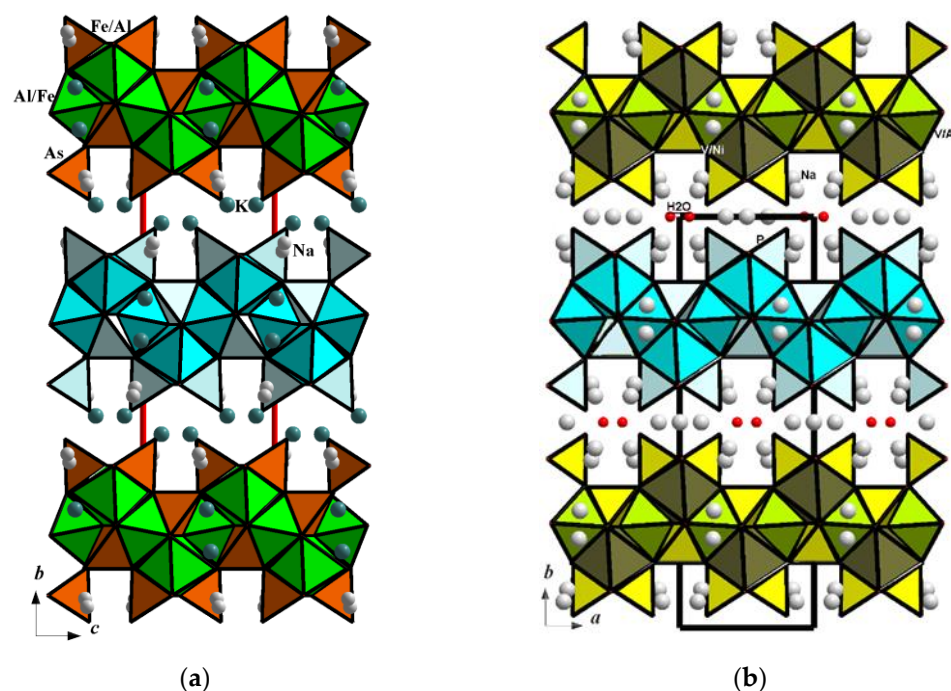
Figure 7. Repeating modules in (**a**) pansnerite, $Na_{1.6}K_{1.4}(Fe^{3+}_{1.65}Al_{1.35})(AsO_4)_4$ and (**b**) $Na_{3.46}(V^{3+}_{1.54}Ni^{2+}_{0.46})^{M1}(V^{3+}_{0.61}Al_{0.39})^{M2}(PO_4)_4(H_2O)$ crystal structures displayed along the axis of about 10.5 Å.

Likewise, the unit cell parameters of about ~21 Å, are inherent to the isotypic minerals ozerovaite, $Na_2KAl_3(AsO_4)_4$ [34], and pansnerite, $K_{1.5}Na_{1.5}Fe^{3+}_3(AsO_4)_4$ [35], the crystal structures of which can also be considered as derivatives of the structure of α-CrPO$_4$. Both orthorhombic minerals were found in the fumaroles of the second scoria cone of the Great Tolbachik fissure eruption, Kamchatka, Russia. According to [35], they were deposited from hot gas as sublimates or formed as a result of the interaction between fumarolic gas and basalt scoria at temperatures not lower than 430–450 °C. Ozerovaite and pansnerite crystallize in the space group *Cmca*; they have many synthetic analogues among arsenates with alkali and transition metals mentioned in [34]. The ozerovaite and pansnerite crystal structures are also built of the bi-periodic slabs, i.e., fragments of the α-CrPO$_4$ archetype.

The main difference between the crystal structures of synthetic phosphates $Na_3V^{3+}_3(PO_4)_4$, $K_3V^{3+}_3(PO_4)_4·H_2O$ and $Na_{3.46}(V^{3+}_{1.54}Ni^{2+}_{0.46})^{M1}(V^{3+}_{0.61}Al_{0.39})^{M2}(PO_4)_4$ (H_2O) on the one hand, and the structures of arsenate minerals ozerovaite and pansnerite, on the other hand, is the arrangement of bi-periodic fragments isolated from the α-CrPO$_4$ structure, along the axis of about 21 Å. As can be seen from Figure 7, the "α-CrPO$_4$" modules, neighboring in the [010] direction in pansnerite, are shifted along the *c* axis compared with the neighboring modules in the title structure.

4. Ionic Conductivity

As discussed previously, the family of α-CrPO$_4$ derivative compounds has shown promise as materials for metal-ion batteries. For this reason, the Na ion migration in the new modification $Na_{3.46}(V^{3+},Ni^{2+})_2(V^{3+},Al)(PO_4)_4·H_2O$ was analyzed to evaluate its potential as an electrode material. Primarily, we assessed the geometric parameters of the crystal structure using the ToposPro package [36] to determine whether there is sufficient space for the migration of Na ions within the structure. The Dirichlet program calculated the free space between the "framework" atoms forming the $(V^{3+},Ni^{2+})_2(V^{3+},Al)(PO_4)_4$ slabs. The water molecule found to be partially populated was excluded from the analysis because it would naturally evaporate through the calcination or charging/discharging

process, as observed for zeolitic water non-bonded to any framework cation, e.g., in $K_3V_3(PO_4)_4 \cdot H_2O$ [31]. Partitioning the free space into Voronoi–Dirichlet polyhedra revealed 38 voids, 7 of which had a radius of at least 1.54 Å and were connected by channels with a width of at least 2.0 Å. As a result, a three-dimensional (3D) percolating network of voids suitable for Na^+-ion migration was identified. Remarkably, all Na atoms in the structure are located in the calculated migration paths, thus allowing all 3,5 Na atoms per formula unit to contribute to conductivity.

3D continuous migration pathways for Na^+ in the $Na_{3.46}(V^{3+},Ni^{2+})_2(V^{3+},Al)(PO_4)_4 \cdot H_2O$ structure were also confirmed by bond valence energy landscapes (BVEL) analysis (Figure 8), and the migration barriers were calculated to be ~0.44 eV along the *a* and *b* directions and ~0.42 eV along the *c* axis. These values are close to those obtained for Na^+ migration in the empty α-VPO_4 [22] framework and suggest that this compound might exhibit ionic conductivity and serve as a potential positive electrode material for sodium-ion batteries if vanadium and/or nickel redox transitions are accessible. The theoretical specific capacity of the presented compound upon deintercalation of all sodium ions is close to 155 mAh/g. However, it seems impossible to achieve such a high level of capacity due to the absence of a rigid three-periodic structure after total removal of Na ions. The bvlain Python package [37,38] was used to determine the bond valence site energies, create the landscapes [39], and calculate ion migration barriers. The bond valence force field parameters are taken from the data provided by He et al. [40].
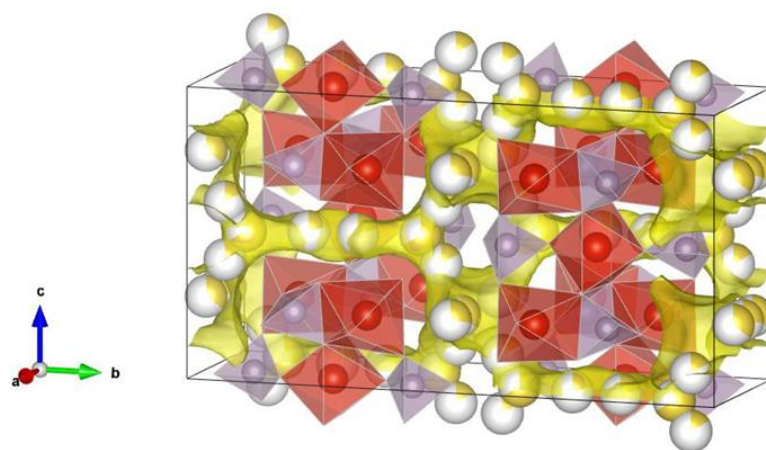

Figure 8. BVEL migration pathways of Na^+ ions (light-grey balls) in the $Na_{3.46}(V^{3+},Ni^{2+})_2(V^{3+},Al)(PO_4)_4 \cdot H_2O$ crystal structure (yellow isosurfaces) with E_{act} set to 0.44 eV illustrated using VESTA 3 software [41]. The phosphate tetrahedra are dark-grey. MO_6 octahedra are shown in red.

5. Conclusions

The sodium vanadium phosphate hydrate, $Na_{3.46}(V^{3+}_{1.54}Ni^{2+}_{0.46})^{M1}(V^{3+}_{0.61}Al_{0.39})^{M2}(PO_4)_4(H_2O)$, was synthesized under high-temperature hydrothermal conditions. Its crystal structure, studied by low-temperature single crystal X-ray diffraction, is discussed as a new member in a series of mineral and synthetic phases derived from the α-$CrPO_4$ archetype, known for a large range of compounds with promising properties. The title structure is formed by intercrossed chains of alternating *M*1- and *M*2-centered octahedra linked via oxygen-bridging contacts. Every $M1O_6$ polyhedron shares two O vertices with $M2O_6$ octahedra to form two-layered slabs perpendicular to the *b* axis of the unit cell. $P2O_4$ tetrahedra share all vertices and one edge with octahedra within the slabs, while one vertex of $P1O_4$ tetrahedra is not shared with octahedra and is directed along the *b* axis in the space between the slabs. A tri-periodic network of voids suitable for Na^+-ion migration was identified within the structure. These continuous migration pathways for Na^+ were

confirmed by the BVEL analysis, and the migration barriers turned out to be about 0.44 eV along the *a* and *b* directions and ~0.42 eV along the *c* axis. These relatively low values within the method indicate the potential of the compound as an electrode material for sodium-ion batteries.

References

1. Krivovichev, S. (Ed.) *Minerals as Advanced Materials I*; Springer: Berlin/Heidelberg, Germany, 2008; 255p, ISBN 978-3-540-77122-7.
2. Krivovichev, S. (Ed.) *Minerals as Advanced Materials II*; Springer: Berlin/Heidelberg, Germany, 2012; 427p. [CrossRef]
3. Masquelier, C.; Croguennec, L. Polyanionic (Phosphates, Silicates, Sulfates) Frameworks as Electrode Materials for Rechargeable Li (or Na) Batteries. *Chem. Rev.* **2013**, *113*, 6552–6591. [CrossRef] [PubMed]
4. Antipov, E.V.; Khasanova, N.R.; Fedotov, S.S. Perspectives on Li and transition metal fluoride phosphates as cathode materials for a new generation of Li-ion batteries. *IUCrJ* **2015**, *2*, 85–94. [CrossRef] [PubMed]
5. Yakubovich, O.V. Phosphates with amphoteric oxo-complexes: From structural features to genetic conclusions. *Z. Kristallogr. Cryst. Mater.* **2008**, *223*, 126–131. [CrossRef]
6. Yakubovich, O.V.; Khasanova, N.R.; Antipov, E.V. Minerals as inspired materials: Synthetic phosphate analogues for battery application. *Minerals* **2020**, *10*, 524. [CrossRef]
7. Kubota, K.; Dahbi, M.; Hosaka, T.; Kumakura, S.; Komaba, S. Towards K-Ion and Na-Ion Batteries as "Beyond Li-Ion". *Chem. Rec.* **2018**, *18*, 459–479. [CrossRef]
8. Peters, J.F.; Peña Cruz, A.; Weil, M. Exploring the economic potential of sodium-ion batteries. *Batteries* **2019**, *5*, 10. [CrossRef]
9. He, M.; Liu, S.; Wu, J.; Zhu, J. Review of cathode materials for sodium-ion batteries. *Prog. Solid State Chem.* **2024**, *74*, 100452. [CrossRef]
10. Delmas, C. Sodium and Sodium-Ion Batteries: 50 Years of Research. *Adv. Energy Mater.* **2018**, *8*, 1703137. [CrossRef]
11. Bauer, A.; Song, J.; Vail, S.; Pan, W.; Barker, J.; Lu, Y. The Scale-up and Commercialization of Nonaqueous Na-Ion Battery Technologies. *Adv. Energy Mater.* **2018**, *8*, 1702869. [CrossRef]
12. Chen, S.; Wu, C.; Shen, L.; Zhu, C.; Huang, Y.; Xi, K.; Maier, J.; Yu, Y. Challenges and Perspectives for NASICON-Type Electrode Materials for Advanced Sodium-Ion Batteries. *Adv. Mater.* **2017**, *29*, 170043. [CrossRef]
13. Serras, P.; Palomares, V.; Goni, A.; Gil de Muro, I.; Kubiak, P.; Lezama, L.; Rojo, T. High voltage cathode materials for Na-ion batteries of general formula $Na_3V_2O_{2x}(PO_4)_2F_{3-2x}$. *J. Mater. Chem.* **2012**, *22*, 22301–22308. [CrossRef]
14. Glaum, R.; Gruehn, R.; Möller, M. Darstellung und Struktur von α-CrPO₄. Beiträge zum thermischen Verhalten von wasserfreien Phosphaten. I. *Z. Anorg. Allg. Chem.* **1986**, *543*, 111–116. [CrossRef]
15. Agilent. *CrysAlis PRO*; Agilent Technologies Ltd.: Yarnton, UK, 2014.
16. Farrugia, L.J. WinGX and ORTEP for Windows: An update. *J. Appl. Crystallogr.* **2012**, *45*, 849–854. [CrossRef]
17. Sheldrick, G.M. *SHELXT*-Integrated Space-Group and Crystal-Structure Determination. *Acta Crystallogr.* **2015**, *A71*, 3–8. [CrossRef]

18. Sheldrick, G.M. Crystal structure refinement with *SHELXL*. *Acta Crystallogr.* **2015**, *C71*, 3–8. [CrossRef]

19. *International Tables for Crystallography*, 3rd ed.; Prince, E., Ed.; Kluwer: Dordrecht, The Netherlands, 2004; Table 4.2.6.8 and 6.1.14.

20. Brown, I.D.; Altermatt, D. Bond-valence parameters obtained from a systematic analysis of the Inorganic Crystal Structure Database. *Acta Crystallogr.* **1985**, *B41*, 244–247. [CrossRef]

21. Brandenburg, K. *DIAMOND*; Crystal Impact GbR: Bonn, Germany, 2006.

22. Fedotov, S.S.; Samarin, A.S.; Nikitina, V.A.; Stevenson, K.J.; Abakumov, A.M.; Antipov, E.V. α-VPO$_4$: A Novel Many Monovalent Ion Intercalation Anode Material for Metal-Ion Batteries. *ACS Appl. Mater. Interfaces* **2019**, *11*, 12431–12440. [CrossRef]

23. Shraer, S.D.; Luchinin, N.D.; Trussov, I.A.; Aksyonov, D.A.; Morozov, A.V.; Ryazantsev, S.V.; Iarchuk, A.R.; Morozova, P.A.; Nikitina, V.A.; Stevenson, K.J.; et al. Development of vanadium-based polyanion positive electrode active materials for high-voltage sodium-based batteries. *Nat. Commun.* **2022**, *13*, 4097. [CrossRef]

24. Shraer, S.; Dembitskiy, A.; Trussov, I.; Komayko, A.; Aksyonov, D.; Luchinin, N.; Morozov, A.; Pollastri, S.; Aquilanti, G.; Ryazantsev, S.; et al. Designing a 3D framework NaVOPO$_4$ as a high-power, low-strain and long-life positive electrode material for Na-ion batteries. *Energy Storage Mater.* **2024**, *68*, 103358. [CrossRef]

25. Kinomura, N.; Matsui, N.; Kumada, N.; Muto, F. Synthesis and Crystal Ctructure of NaV$_3$P$_3$O$_{12}$: A Stuffed Structure of α-CrPO$_4$. *J. Solid State Chem.* **1989**, *79*, 232–237. [CrossRef]

26. Wang, X.; Hu, P.; Chen, L.; Yao, Y.; Kong, Q.; Cui, G.; Shi, S.; Chen, L. An α-CrPO$_4$-type NaV$_3$(PO$_4$)$_3$ Anode for Sodium-Ion Batteries with Excellent Cycling Stability and the Exploration of Sodium Storage Behavior. *J. Mater. Chem. A* **2017**, *5*, 3839–3847. [CrossRef]

27. Ishado, Y.; Inoishi, A.; Okada, S. Exploring Factors Limiting Three-Na$^+$ Extraction from Na$_3$V$_2$(PO$_4$)$_3$. *Electrochemistry* **2020**, *88*, 457–462. [CrossRef]

28. Britvin, S.N.; Murashko, M.N.; Krzhizhanovskaya, M.G.; Vapnik, Y.; Vlasenko, N.S.; Vereshchagin, O.S.; Pankin, D.V.; Zaitsev, A.N.; Zolotarev, A.A. Yakubovichite, CaNi$_2$Fe^{3+}(PO$_4$)$_3$, a New Nickel Phosphate Mineral of Non-Meteoritic Origin. *Am. Mineral.* **2023**, *108*, 2142–2150. [CrossRef]

29. Ouaatta, S.; Assani, A.; Saadi, M.; El Ammari, L. Crystal structure of calcium dinickel(II) iron(III) tris(orthophosphate): CaNi$_2$Fe(PO$_4$)$_3$. *Acta Crystallogr.* **2017**, *E73*, 893–895. [CrossRef]

30. Rouse, R.C.; Peacor, D.R.; Metz, G.W. Sverigeite, a structure containing planar NaO4 groups and chains of 3- and 4-membered beryllosilicate rings. *Am. Mineral.* **1989**, *74*, 1343–1350.

31. Jenkins, T.; Alarco, J.A.; Mackinnon, I.D.R. Synthesis and characterization of a Novel Hydrated Layered Vanadium(III) Phosphate Phase K$_3$V$_3$(PO$_4$)$_4 \cdot$H$_2$O: A Functional Cathode Material for Potassium-Ion Batteries. *ACS Omega* **2021**, *6*, 1917–1929. [CrossRef]

32. Liu, R.; Liu, H.; Sheng, T.; Zheng, S.; Zhong, G.; Zheng, G.; Liang, Z.; Ortiz, G.F.; Zhao, W.; Mi, J.; et al. Novel 3.9 V Layered Na$_3$V$_3$(PO$_4$)$_4$ Cathode Material for Sodium Ion Batteries. *ACS Appl. Energy Mater.* **2018**, *1*, 3603–3606. [CrossRef]

33. Alkhateeban, A.; BenYahia, H. Investigation of the inorganic compounds NaMV$_2$(PO$_4$)$_3$ (M=Fe, Co, Ni) as anode materials for sodium-ion batteries. *ACS Omega* **2020**, *5*, 30799–30807. [CrossRef]

34. Shablinskii, A.P.; Filatov, S.K.; Vergasova, L.P.; Avdontseva, E.Y.; Moskaleva, S.V.; Povolotskiy, A.P. Ozerovaite, Na$_2$KAl$_3$(AsO$_4$)$_4$, new mineral species from Tolbachik volcano, Kamchatka peninsula, Russia. *Eur. J. Mineral.* **2019**, *31*, 159–166. [CrossRef]

35. Pekov, I.V.; Zubkova, N.V.; Koshlyakova, N.N.; Agakhanov, A.A.; Belakovskiy, D.I.; Vigasina, M.F.; Yapaskurt, V.O.; Britvin, S.N.; Turchkova, A.G.; Sidorov, E.G.; et al. New arsenate minerals from the Arsenatnaya fumarole, Tolbachik volcano, Kamchatka, Russia. XIII. Pansnerite, K$_3$Na$_3$Fe$^{3+}_6$(AsO$_4$)$_8$. *Mineral. Mag.* **2020**, *84*, 143–151. [CrossRef]

36. Blatov, V.A.; Shevchenko, A.P.; Proserpio, D.M. Applied Topological Analysis of Crystal Structures with the Program Package ToposPro. *Cryst. Growth Des.* **2014**, *14*, 3576–3586. [CrossRef]

37. Dembitskiy, A.D.; Aksyonov, D.A.; Abakumov, A.M.; Fedotov, S.S. NH$_4^+$-based frameworks as a platform for designing electrodes and solid electrolytes for Na-ion batteries: A screening approach. *Solid State Ion.* **2022**, *374*, 115810. [CrossRef]

38. BVlain Python Package. Available online: https://github.com/dembart/BVlain (accessed on 19 December 2024).

39. Adams, S.; Rao, R.P. High power lithium-ion battery materials by computational design. *Phys. Status Solidi* **2011**, *A208*, 1746–1753. [CrossRef]

40. He, B.; Ye, A.; Chi, S.; Mi, P.; Ran, Y.; Zhang, L.; Zou, X.; Pu, B.; Zhao, Q.; Zou, Z.; et al. CAVD, towards better characterization of void space for ionic transport analysis. *Sci. Data* **2020**, *7*, 153. [CrossRef]

41. Momma, K.; Izumi, F. VESTA 3 for three-dimensional visualization of crystal, volumetric and morphology data. *J. Appl. Cryst.* **2011**, *44*, 1272–1276. [CrossRef]